AIAA 99–1020

Subsonic Static and Dynamic Aerodynamics of Blunt Entry Vehicles

Robert A. Mitcheltree , Charles M. Fremaux,
NASA Langley Research Center, Hampton, Virginia
Leslie A. Yates,
AerospaceComputing, Los Altos, California

37th Aerospace Sciences Meeting and Exhibit
January 11–14, 1999/Reno, Nevada

For permission to copy or republish, contact the American Institute of Aeronautics and Astronautics
1801 Alexander Bell Drive, Suite 500, Reston, VA 22091

Subsonic Static and Dynamic Aerodynamics of Blunt Entry Vehicles

Robert A. Mitcheltree *, Charles M. Fremaux,†
NASA Langley Research Center, Hampton, Virginia
Leslie A. Yates,‡
AerospaceComputing, Los Altos, California

The incompressible subsonic aerodynamics of four entry-vehicle shapes with variable c.g. locations are examined in the Langley 20-Foot Vertical Spin Tunnel. The shapes examined are spherically-blunted cones with half-cone angles of 30, 45, and 60 deg. The nose bluntness varies between 0.25 and 0.5 times the base diameter. The Reynolds number based on model diameter for these tests is near 500,000. Quantitative data on attitude and location are collected using a video-based data acquisition system and reduced with a six deg-of-freedom inverse method. All of the shapes examined suffered from strong dynamic instabilities which could produced limit cycles with sufficient amplitudes to overcome static stability of the configuration. Increasing cone half-angle or nose bluntness increases drag but decreases static and dynamic stability.

Nomenclature

A_1, A_2, A_3 = coefficients in velocity fit (Eq. 5)
C_D = drag force coefficient
$C_{D,0}, C_{D_{\alpha^2}}$ = drag force coefficient terms (Eq. 1)
C_L = Lift force coefficient
$C_{L_0}, C_{L_\alpha}, C_{L_{\alpha^3}}$ = lift coefficient terms (Eq. 2)
C_m = moment coefficient referenced to c.g.
$C_{m_0}, C_{m_\alpha}, C_{m_{\alpha^3}}$ = moment coefficient terms (Eq. 3)
C_{m_q} = dynamic damping derivative
$C_{m_{q,0}}, C_{m_{q,\alpha^2}}$ = damping derivative terms (Eq. 4)
$C^*_{m_q}$ = simplified dynamic stability parameter (Eq. 6)
D = maximum body diameter, m
I_x = moment of inertia about the x-axis, $kg - m^2$
I_y = moment of inertia about the y-axis, $kg - m^2$
I_z = moment of inertia about the z-axis, $kg - m^2$
M = model mass, kg
N = model to vehicle length scale factor
Re_D = Reynolds number based on diameter
R_n = model nose radius, m
t = time, sec
V = free stream velocity, m/s
x, y, z = coordinate directions, m
$z_{c.g.}$ = distance center-of-gravity is aft of nose, m
α - total angle of attack, $deg.$
Θ = Pitch angle, $deg.$
Ψ = Yaw angle, deg
σ = ratio of air density at altitude to that at sea level
ν = kinematic viscosity at altitude, m^2/s^2
ν_0 = kinematic viscosity at sea level, m^2/s^2
λ = radius of gyration $\sqrt{I_x/M}$, m

Introduction

Selection of the aeroshell shape for an entry vehicle is usually driven by the need for high aerodynamic drag, low aerothermal heating, and sufficient aerodynamic stability. Fortunately, shapes such as blunted, large-angle cones which have high drag also minimize the aerothermal heating environment. Blunted large angle cones, however, can suffer aerodynamic stability problems if the packaging of the vehicle's payload can not position the center-of-gravity (c.g.) close to the vehicle's nose.

The aerodynamic stability of a blunted, large-angle cone varies across the speed regimes. At hypersonic continuum conditions, blunt shapes exhibit acceptable stability even for a c.g. position behind the maximum diameter location of the aeroshell. At transonic speeds, such a c.g. position is accompanied by a bounded dynamic instability[1,2] which will induce oscillatory motions. At subsonic speeds, the strength of the dynamic instability can overcome the static stability causing the vehicle's oscillations to diverge into a tumbling motion.[3] Therefore, the c.g. requirement for an entry vehicle whose entry profile includes subsonic flight is driven by the subsonic dynamic stability of the aeroshell.

The low-speed dynamics of blunt entry vehicle shapes were studied in the late 1960's and early 1970's as the planetary entry probes for Mars-Viking, Pioneer-Venus, and Galileo-Jupiter were designed. These studies included tests in the NASA Langley 20-Foot Vertical Spin Tunnel[4-6], horizontal wind tunnels[7,8], drop tests[9,10], and flight tests[11]. As the erratic dynamic behavior of high-drag bodies in subsonic

*Aerospace Engineer, Aerothermodynamics Branch, Aero- and Gas Dynamics Division, NASA Langley Research Center, Senior Member AIAA.
†Aerospace Engineer, Vehicle Dynamics Branch, Flight Dynamics and Control Division, NASA Langley Research Center, Senior member AIAA.
‡Vice President Aerospace Computing, Los Altos, CA., Senior member AIAA

Copyright ©1999 by the American Institute of Aeronautics and Astronautics, Inc. No copyright is asserted in the United States under Title 17, U.S. Code. The U.S. Government has a royalty-free license to exercise all rights under the copyright claimed herein for governmental purposes. All other rights are reserved by the copyright owner.

Table 1 Model Geometry, Mass and c.g. Location

Case	Cone (deg)	R_n/D	M, kg	$z_{c.g.}/D$
3050a	30	0.50	1.378	0.357
3050b	30	0.50	1.377	0.329
4525b	45	0.25	1.373	0.354
4525c	45	0.25	1.355	0.324
4550b	45	0.50	1.355	0.250
4550c	45	0.50	1.370	0.266
6025a	60	0.25	1.552	0.230
6025b	60	0.25	1.481	0.246

(and transonic) flows was revealed, entry systems designers sometimes chose to avoid these flight regimes by deploying parachutes at supersonic speeds. These earlier studies also revealed the necessity of dynamic testing to determine the stability of blunt shapes in transonic and subsonic flows. A vehicle whose static stability appears acceptable from static-sting mounted wind tunnel tests may possess dynamic instabilities which can lead to unacceptable or divergent behavior in flight[3].

The objective of the present work is to examine the incompressible subsonic dynamics of four entry-vehicle shapes with variable c.g. locations in the Langley 20-Foot Vertical Spin Tunnel. The shapes examined are spherically-blunted cones with half-cone angles of 30, 45, and 60 deg. The nose bluntness varies between 0.25 and 0.5 times the base diameter. Quantitative data on model attitude and position are collected using a video-based data acquisition system and reduced with a six deg-of-freedom (6DOF) inverse method. Representative data at two c.g. locations for each shape are presented as well as the results of the data reduction calculations.

Geometries and Dynamically-Scaled Models

The four geometries examined are the spherically blunted cones presented in Fig.1. Two different c.g. locations are examined for each geometry. The c.g. locations selected are on the geometric symmetry axis and positioned just forward of the neutral dynamic stability point. C.g. locations are measured from the actual nose of the model. The eight cases for which data collection and reduction are performed are listed in Table 1. The first entry in the table is the case designator. Table 2 presents the associated moments of inertia.

The models were constructed of high density foam and fiberglass in two sections. All models used a common after body section which included the mechanism to vary the model's c.g. location. The maximum diameter of all models was 0.355 m and each had a shoulder radius (between forebody and afterbody) of 0.009 m.

Table 2 Model Mass Inertias

Case	I_x (kg-m^2)	I_y (kg-m^2)	I_z (kg-m^2)
3050a	0.0113	0.0108	0.0159
3050b	0.0108	0.0103	0.0159
4525b	0.0104	0.0101	0.0152
4525c	0.0109	0.0103	0.0137
4050b	0.0104	0.0099	0.0152
4550c	0.0104	0.0099	0.0152
6025a	0.0105	0.0099	0.0182
6025b	0.0105	0.0098	0.0176

Table 3 Dynamic Scaling Relationships

Parameter	Scale Factor
Linear Dimension	N
Relative Density	1
Froude Number	1
Mass	N^3/σ
Moment of Inertia	N^5/σ
Linear Velocity	$N^{1/2}$
Linear Acceleration	1
Angular Velocity	$1/N^{1/2}$
Time	$N^{1/2}$
Reynolds Number	$N^{3/2}\nu/\nu_0$

Inertias were adjusted by the addition of weights to represent scaled flight values of designs with centrally positioned payloads. Free flying models tested in the Spin Tunnel can be dynamically scaled using the dynamic scaling parameters in Table 3. The dimensions of mass, length, and time are scaled so that the model results may be applied directly to predict the behavior of a full-scale vehicle. In this process, time is scaled on the basis of equal Froude number, length on the basis of similar geometry, and mass properties by assuming equal relative density, (i.e., the ratio of vehicle density to air density at the desired altitude). Full scale values are obtained by dividing model values by the listed scale factors. A detailed discussion of dynamic scaling may be found in Ref. 12.

The Reynolds numbers based on model diameter for the present tests were 440,000 to 526,000. The backwards facing step afterbody was chosen to anchor flow seperation points in an attempt to minimize Reynolds number effects.

Vertical Spin Tunnel and Data Acquisition

The Langley 20-Foot Vertical Spin Tunnel is an atmospheric, annular return, vertical wind tunnel. The test section is 20 feet across and 25 feet in length. A 400 hp electric motor (1300 hp for short periods) turns a 3-bladed, fixed pitch fan to produce speeds of up to

27 m/s, with a maximum acceleration and deceleration capability of 4.6 m/s^2 and 7.6 m/s^2, respectively. The present tests were run at speeds between 18 and 22 m/s. Figure 2 presents a schematic of the facility. A complete description may be found in Ref. 13.

For the tests, a lightweight tether system was used to reduce model damage from impact with the tunnel walls. A smooth metal ring was suspended in the center of the test section using guy wires. The tether was attached to the rear face of the after body, routed through the metal ring, and attached to the tunnel wall. At the beginning of a test, the model was suspended on the tether with the tunnel fan stopped. As the tunnel was brought up to speed, the tether became slack when model drag equaled the model weight (see Fig. 2). The tether appeared to have little influence on the model motions.

Standard videotapes are made to document each test and aid in qualitative analysis. However, primary data for tests of free-flying models are 6 degree-of-freedom (6DOF) motion time histories, obtained via the Spin Tunnel Model Space Positioning System (MSPS). The MSPS is a non-intrusive, computer workstation-based system that uses two video camera views of retro-reflective targets attached to known locations on a model to generate post-test estimates of model attitude and position at a sample rate of 60 Hz. The angles of oscillations are pitch and yaw consistent with aircraft definitions where the nose of the equivalent aircraft is at the nose of the capsule. The accuracy of angles reported by MSPS is within plus or minus one deg of the actual values. However, due to the small size of the models (diameter of 0.355 m), the accuracy of the system was degraded. No error analysis for the current tests was performed, but it is believed that the angle values reported in this document are to within plus or minus two deg.

Data acquisition using the MSPS system begins at a time specified by the operator during a test run. As such, the beginning of the plots (t=0) contained in this report corresponds to an arbitrary point in the test but often followed an intentional perturbation of model attitude. For the present tests, loss of track sometimes occurred when the model was rolled or pitched to such a large angle that the targets were no longer visible. Visual review of the corresponding test videotape is used to supplement the data provided by MSPS for this purpose. Reference 14 provides further discussion of the MSPS system.

Test section velocity is not recorded by the video-based MSPS system. It can be obtained using pitot-static pressure probes as well as a temperature probe protruding from the tunnel walls. The calculated airspeed is used to determine the average equilibrium sink rate of the free-flying model. Velocity is varied during the test to maintain the model in the test section.

Data Reduction

The MSPS position and attitude data for each case were analyzed using a 6 degree-of-freedom parameter identification routine, CADRA2[15]. For the present application, CADRA2 identifies parameters in expressions for the aerodynamic coefficients utilizing the nonlinear approach outlined in Ref. 16. The expressions for the aerodynamic coefficients for this axisymmetric, low speed study are:

$$C_D = C_{D_0} + C_{D_{\alpha^2}} sin^2\alpha \tag{1}$$

$$C_L = C_{L_0} + C_{L_\alpha} sin\alpha + C_{L_{\alpha^3}} sin^3\alpha \tag{2}$$

$$C_m = C_{m_0} + C_{m_\alpha} sin\alpha + C_{m_{\alpha^3}} sin^3\alpha \tag{3}$$

$$C_{m_q} = C_{m_{q,0}} + C_{m_{q,\alpha^2}} sin^2\alpha \tag{4}$$

where the usual Mach number terms, used in ballistics range studies, have been omitted. The absence of time-varying velocity information in the data introduced difficulties in the identification of the nonlinear terms. Consequently, the data were also reduced assuming linear aerodynamics by neglecting the higher order terms in the above expressions.

In an attempt to discern the velocity variations and reveal the nonlinear aerodynamics, the velocity was modeled as

$$V = V_0 + \frac{dz}{dt} + A_1 t + A_2 t^2 + A_3 t^3 \tag{5}$$

with the coefficients of this expression added to the list of parameters to be identified by CADRA2.

Due to the uncertainty in velocity variations during the test, the estimated errors for the coefficients predicted are 10% for drag, 5% for moment coefficient, and plus or minus 0.01 for the damping coefficients.

Stability, Limit Cycles, and Divergence

Stability can be defined in various ways, however, defining the acceptable stability for nonlinear systems such as oscillating aeroshells is difficult. Typically, when the c.g. location of an aeroshell (like those shown in Fig. 1) is very close to its nose, the vehicle displays stable subsonic behavior. Any perturbation in attitude is decayed until it vanishes. As the c.g. is moved aft from the nose, a marginally stable behavior emerges in which a limit cycle oscillation exists. In addition, the stability of most blunt aeroshells will bifurcate into bistability: capable of stable flight in both a forward and backwards orientation. At this point, the amplitude of a perturbation from which the vehicle can successfully return to a forward facing attitude becomes bounded. As the c.g. location is moved further aft, the amplitude of the limit cycle increases and the amplitude of a allowable perturbation which returns to a forward orientation decreases. As the c.g. is moved even further aft, an initially forward orientation will diverge into a

tumbling motion which, depending on the afterbody shape, may or may not seek a backwards orientation.

The oscillatory motion of a blunt entry vehicle in subsonic terminal descent is analogous to that of a nonlinear mass-spring-damper system. In this analogy, static stability corresponds to the spring stiffness and dynamic stability corresponds to the damper's characteristics. The dynamic damping of an aeroshell is highly nonlinear and can be destabilizing at small angle-of-attack and stable for larger angles which (if statically stable) leads to limit cycle behavior. The amplitude of the limit cycle and the amplitude of a perturbation which does not result in a tumbling motion is a function of the dynamic stability, the static stability, and the mass properties of the vehicle.

Results and Observations

The pitch, Θ, and yaw, Ψ, angles measured in the eight cases examined are presented in Figs. 3-10. In most cases, the model was perturbed prior to $t = 0$ and the motion presented is the decay of that perturbation. For clarity, the 60-Hz discrete data is presented in line form. Gaps during data collection produce the interspersed linear segments in Figs 5,6,7, and 10.

Figures 3 and 4 present the oscillations observed for two different c.g. locations for the 30-deg half angle cone with nose radius equal to half of the base diameter (configuration 3050). The large amplitude of the oscillations in figure 3 is an indication of the size of the initial perturbation prior to data collection. Comparison of the frequency of oscillation between Fig. 3 and Fig. 4 indicates that both c.g. locations are statically stable with Fig. 4 indicating the higher frequency (larger negative $C_{m,\alpha}$).

Despite the aparent growth in Ψ in Fig. 4, the amplitutde of the total angle-of-attack oscillation is decaying in Fig. 3 and 4. This decay indicates dynamically stable configurations. Reducing this data with linear and nonlinear aerodynamic coefficients and fits to the velocity variations produced minimal differences in the predicted aerodynamics. The data do not indicate the vehicle is in a limit cycle. The amplitude of the limit cycle, if one exists, is smaller than the angles measured during the test. Table 4 presents a prediction of the aerodynamic coefficients assuming linear coefficients and no velocity variation. Table 5 present the predictions when the velocity model of Eq. 5 is used. The value presented as damping is the term:

$$C^*_{m,q} = C_{m,q} - \left(\frac{\lambda}{D}\right)^2 C_{L,\alpha} \qquad (6)$$

$C^*_{m,q}$ is a simplified form of the dynamic stability parameter for terminal descent.[19] If it is negative the oscillations are damped and decaying. The values for $C^*_{m,q}$ given in Tables 4 and 5 are average values for the current state of the oscillations. Assuming a linear variation in $C^*_{m,q}$ with c.g. location results in a prediction for the neutrally dynamic stability for a c.g. location at 0.387 diameters back from the nose for this 30-deg half-angle geometry. The location of maximum diameter is 0.373 diameters back from the nose.

Figures 5 and 6 present the oscillations associated with the 45 deg half-angle cone model whose nose radius is 0.25 times the base diameter. The oscillations in Fig. 5 show no indication of decay. This geometry and c.g. combination is either unstable or seeking a limit cycle whose amplitude is slightly larger than the amplitude of the observed oscillations: a fact confirmed by the slightly positive value for $C^*_{m,q}$ in Table 4. The amplitude of the final limit cycle this c.g. location will produce for this geometry is estimated at 20 - 25 deg. Both of these cases appear to have large velocity variations during the test period. Since the velocity was not recorded as part of the data, the 6DOF data reduction is unable to distinguish non linear aerodynamic coefficient variations. A prediction of the neutral dynamic stability point is for a c.g. location of 0.346. This extrapolation compares favorably with a qualitative observation of the c.g. location behind which divergence occurs. In particular, for c.g. locations at 0.325 diameters, all perturbations were damped. For c.g. locations at 0.345 to 0.358 diameters, small perturbations damped while large variations diverged. When the c.g. position was positioned at 0.391 diameters back from the nose, the model diverged without perturbation. The location of maximum diameter is 0.407 diameters back from the nose.

Figures 7 and 8 present the oscillation for the 45 deg half angle cone with nose radius equal to half of the base diameter. The values predicted for $C^*_{m,q}$ in Table 4 are both negative, and the observation of the motions during the test indicate that these were both non-divergent configurations (i.e. bounded limit cycles). The trend of dynamic damping with c.g. location for configuration 4550 in Table 4, however, is incorrect. This reversal is due to the uncertainty in the data reduction for this parameter. It is not possible to extrapolate these quantitative values to determine the neutral dynamic stability c.g. location. Additional variation of the model's c.g. location to further aft positions (i.e. test cases not listed in Table 1) revealed that for c.g. locations at 0.274 and .278 diameters back from the nose, the vehicle assumed a limit cycle after small perturbations but could diverge after large perturbations. For a c.g. location of 0.288, the model diverged without perturbation. The location of the maximum diameter is 0.303 diameters back from the nose.

Figures 9 and 10 present the 60 deg half-angle cone cases. For both c.g. locations examined, the models appear to be at or near limit cycle behavior with amplitude 25-30 deg. Again the trend in $C^*_{m,q}$ is reversed making it impossible to predict the c.g. location

Table 4 Aerodynamic Coefficients: :Linear results without velocity variations

Case	$z_{c.g.}/D$	$C_{D,0}$	$C_{m,\alpha}$	$C^*_{m,q}$
3050a	0.357	0.5011	-0.0984	-0.015
3050b	0.329	0.5083	-0.1122	-0.029
4525b	0.354	0.6218	-0.0791	+0.005
4525c	0.324	0.5973	-0.0923	-0.013
4550b	0.250	0.6820	-0.1459	-0.005
4550c	0.266	0.6606	-0.1295	-0.010
6025a	0.230	0.7537	-0.1187	+0.003
6025b	0.246	0.7150	-0.1068	+0.002

Table 5 Aerodynamic Coefficients: :Linear results with velocity variation

Case	$z_{c.g.}/D$	$C_{D,0}$	$C_{m,\alpha}$	$C^*_{m,q}$
3050a	0.357	0.5069	-0.0984	-0.018
3050b	0.329	0.4809	-0.1098	-0.027
4525b	0.354	0.6251	-0.0794	+0.004
4525c	0.324	0.5988	-0.0924	-0.016
4550b	0.250	0.6681	-0.1434	-0.004
4550c	0.266	0.6512	-0.1276	-0.009
6025a	0.230	0.7554	-0.1187	+0.003
6025b	0.246	0.7072	-0.1060	+0.002

for neutral dynamic stability. Variation in c.g. location from additional testing indicate a neutral stability point near 0.260 diameters back from the nose. This value is smaller than the 0.29 value determined in Ref. 3 for a geometry with the same forebody shape but larger afterbody shell. (The radius of gyration normalized by diameter (λ/D) for the present model was 0.230 compared to the larger value of 0.252 examined in Ref. 3.) The location of maximum diameter for this geometry is 0.265 diameters back from the nose.

A static wind tunnel test of the 60-deg half angle cone in Ref. 18, at $Re_D = 1 \times 10^6$, predicted a zero angle drag coefficient of 0.81 which is higher than the present prediction of $0.70 - 0.75$.

The effect of cone half angle and nose bluntness on drag is presented in Fig. 11. Figure 12 compares the static stability of the eight cases examined as a function of c.g. location. In this figure, the two c.g. locations for each model are connected with a line and labeled with the geometry identifier from Table 1. A similar comparison for the dynamic damping parameter is presented in Fig. 13. When comparing stability of two different shapes, it should be remembered that the length from nose to maximum diameter is different for each shape.

Attempts to extract nonlinear aerodynamic coefficients from the data were suspect as a result of the interaction with velocity variation. The inclusion of nonlinear terms from Eqs. 1-4 did little to improve the fits to the data. In addition, with the large amplitude motions exhibited by many of the tests, higher order terms may be required in Eqs 1-4

Conclusions

The incompressible subsonic aerodynamics of four entry-vehicle shapes with variable c.g. locations were examined in the Langley 20-Foot Vertical Spin Tunnel. Quantitative data on attitude and position are collected using a video-based data acquisition system and reduced with a six deg-of-freedom (6DOF) inverse method.

Subsonic drag increases with increasing cone half-angle and nose bluntness. The drag coefficient of a 45 degree half-angle cone is 33 percent higher than a 30 degree half-angle cone when both have a nose radius equal to half their base diameter. A 60 deg cone exhibits 20 percent higher drag than a 45-deg cone when both have a nose radius equal to 0.25 times their base diameter. For a 45 deg half-angle cone, increasing the nose radius from 0.25 to 0.50 times the diameter increases the drag 10 percent.

Static stability, as measured by the magnitude of the moment coefficient slope, decreases with movement of the c.g. away from the nose. This decrease in stability occurs more rapidly when the cone half-angle or the degree of nose bluntness is increased.

The ability of a statically stable blunt shape to decay perturbations (its dynamic stability) decreases with movement of the c.g. away from the nose. Decreased dynamic stability is accompanied by the emergence of limit cycle oscillations. The amplitude of these oscillations increase with movement of the c.g. away from the nose. In addition, the magnitude of a perturbation which does not result in divergence decreases with movement of the c.g. away from the nose. All of the shapes examined suffered from strong dynamic instabilities which (if the c.g. was moved sufficiently back from the nose) could produce limit cycles with sufficient amplitudes to overcome static stability of the configuration. In particular, the onset of uncontrolled tumbling motion was caused by dynamic instabilities even while the models possessed static stability.

The use of a parameter identification routine to extract non-linear aerodynamic coefficients from free flight motion histories from a vertical wind tunnel, requires simultaneous measurement of the velocity variations. In addition, the expressions for the aerodynamic coefficients may require high order terms than considered in the present work.

References

[1]Uselton, B. L.; Shadow, T. O.; and Mansfield, A. C.: "Damping in Pitch Derivatives of 120 and 140 Deg Blunted Cones at Mach Numbers 0.6 through 3.0," AEDC TR-70-49, 1970.

[2]Marko, W. J.:"Transonic Dynamic and Static Stability Characteristics of Three Blunt-Cone Planetary Entry Shapes," NASA CR-107405, JPL TR 32-1357, Sept., 1969.

[3]Mitcheltree, R. A., and Fremaux, C. M., "Subsonic Dynamics of Stardust Sample Return Capsule," NASA TM 110329, March, 1997.

[4]Bendura, R. J.:"Low Subsonic Static and Dynamic Stability Characteristics of Two Blunt 120^0 Cone Configurations," NASA TN D-3853, Feb., 1967.

[5]Costigan, P. J.:"Dynamic-Model Study of Planetary-Entry Configurations in the Langley Spin Tunnel," NASA TN D-3499, July, 1966.

[6]Cahen, G. L.: "Effects of Shape and Mass Properties on Subsonic Dynamics of Planetary Probes," *Journal of Spacecraft and Rockets*, Vol. 12, No. 8, Aug., 1975.

[7]Marte, J. E.; and Weaver, R. W.:"Low Subsonic Dynamic-Stability Investigation of Several Planetary-Entry Configurations in a Vertical Wind Tunnel (Part I)," JPL TR 32-743, May, 1965.

[8]Jaffe, P.:"Terminal Dynamics of Atmospheric Entry Capsules," *AIAA Journal*, Vol. 7, No. 6, June, 1969.

[9]Cassanto, J. M.; and Buce, P.:"Free Fall Stability and Base Pressure Drop Tests for Planetary Entry Configurations," *Journal of Spacecraft and Rockets*, Vol. 8, No. 7, July, 1971.

[10]Jaffe, P.:"Dynamic Stability Tests of Spinning Entry Bodies in the Terminal Regime," *Journal of Spacecraft and Rockets*, Vol. 8, No. 6, June, 1971.

[11]Whitlock, C. H.; and Bendura, R. J.:"Dynamic Stability of a 4.6-meter Diameter 120^0 Conical Spacecraft at Mach Numbers From 0.78 to 0.48 in a Simulated Martian Atmosphere," NASA TN D-4558, May, 1968.

[12]Wolowicz, C. H.; Bowman, J. S.; and Gilbert, W. P.:"Similitude Requirements and Scaling Relationships as Applied to Model Testing," NASA TP 1435, 1979.

[13]Neihouse, A. I.; Kliner, W. J.; and Scher, S. H.:"Status of Spin Research for Recent Airplane Designs," NASA TR R-57, 1960.

[14]Snow, W. L.; Childers, B. A.; Jones, S. B.; and Fremaux, C. M.:"Recent Experiences with Implementing a Video Based Six Degree of Freedom Measurement System for Airplane Models in a 20-Foot Diameter Vertical Spin Tunnel," Proceedings of the SPIE Videometrics Conference, Vol. 1820, 1992, pp. 158-180.

[15]Yates, L. A., and Chapman, G. T., "A Comprehensive Automated Aerodynamic Reduction System for Ballistic Ranges," WL-TR-96-7059, Wright Laboratory, Armament Directorate, Oct. 1996.

[16]Chapman, G. T., Kirk, D. B., "A Method for Extracting Aerodynamic Coefficients From Free-Flight Data," AIAA J., Vol 8, No 4, pp 753-758, April 1970.

[17]Chapman, G. T., Yates, L. A., "Dynamics of Planetary Probes: Design and Testing Issues," AIAA 98-0797, Jan. 1998.

[18]Mitcheltree, R. A., Stardust Aero Database paper

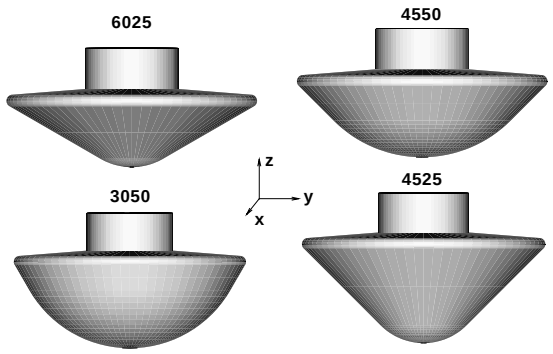

Fig. 1 Four geometries examined and their nomenclature (cone half angle/nose bluntness ratio).

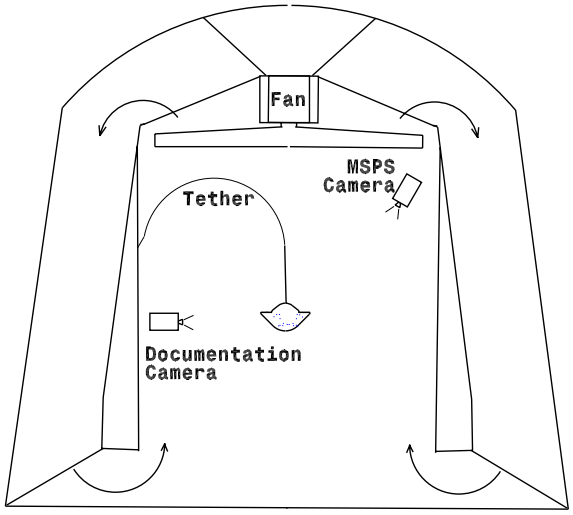

Fig. 2 Schematic of 20-Foot Vertical Spin Tunnel

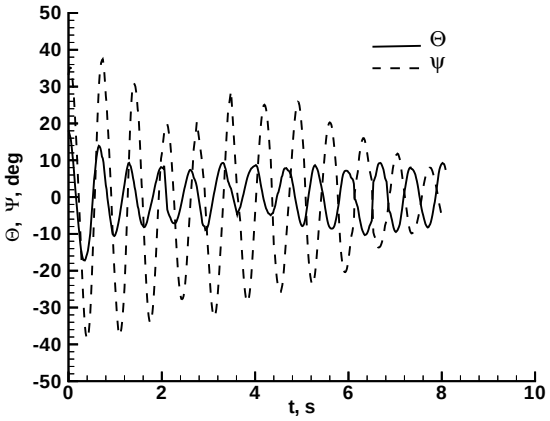

Fig. 3 Pitch and Yaw from test for case 3050a

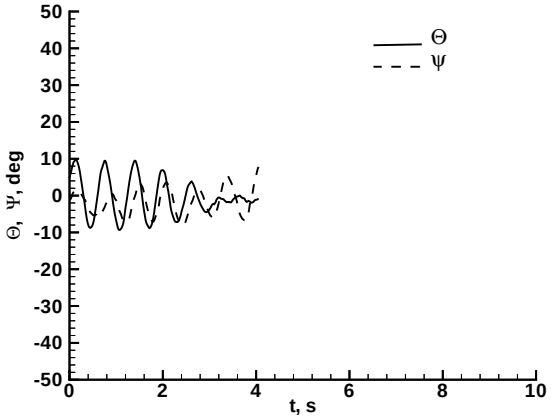

Fig. 4 Pitch and Yaw from test for case 3050b

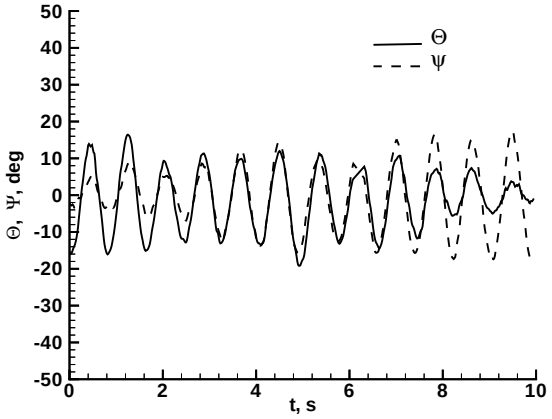

Fig. 5 Pitch and Yaw from test for case 4525b

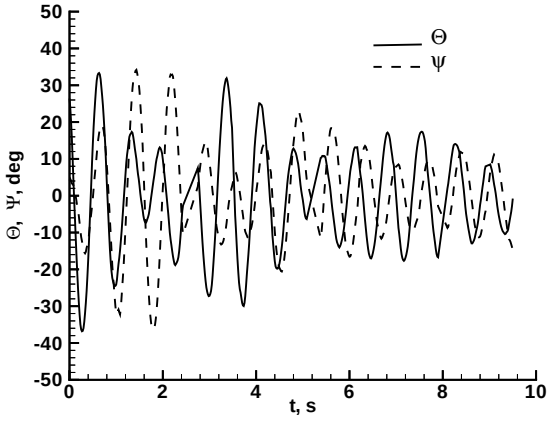

Fig. 6 Pitch and Yaw from test for case 4525c

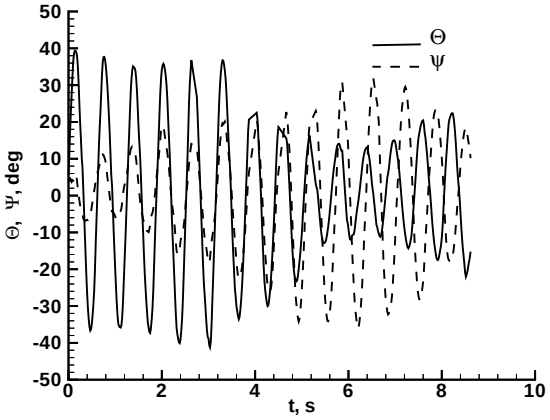

Fig. 7 Pitch and Yaw from test for case 4550b

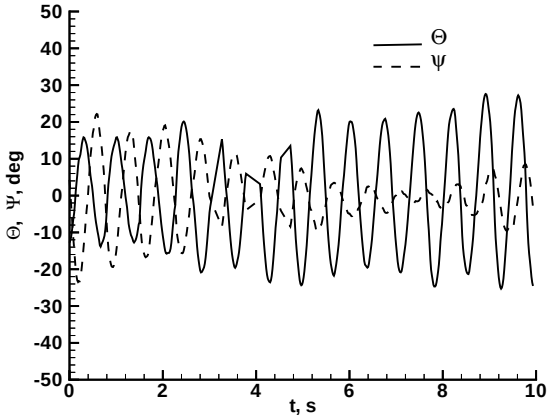

Fig. 10 Pitch and Yaw from test for case 6025b

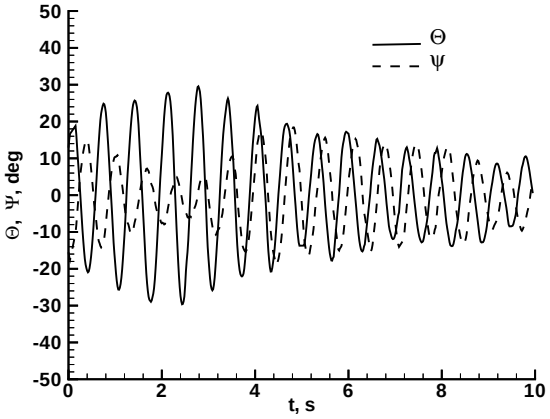

Fig. 8 Pitch and Yaw from test for case 4550c

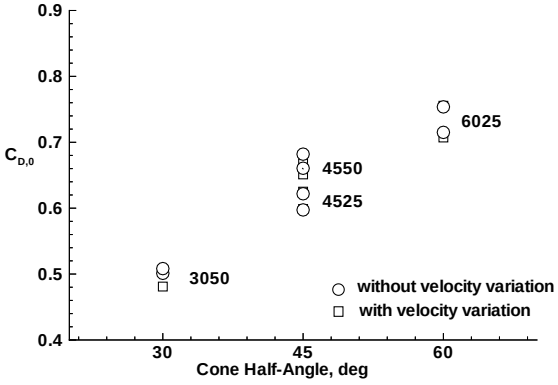

Fig. 11 Variation in drag coefficient with cone half-angle

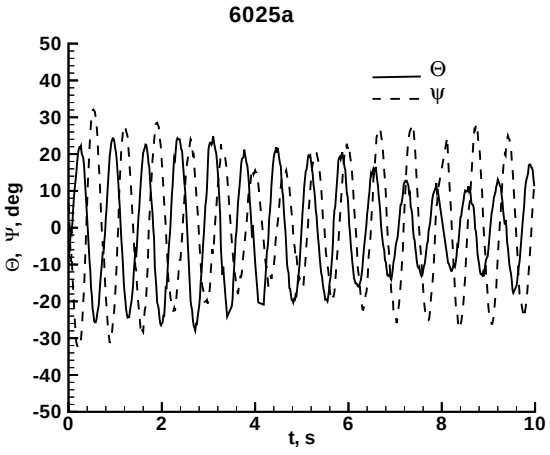

Fig. 9 Pitch and Yaw from test for case 6025a

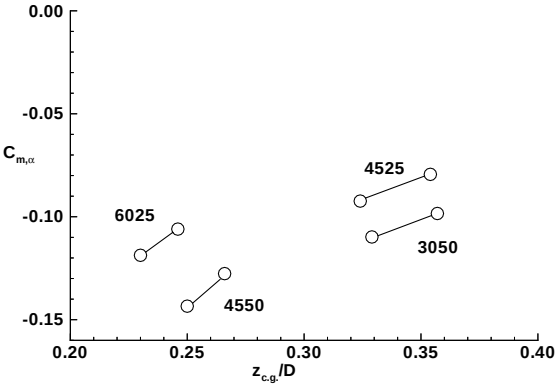

Fig. 12 Variation in moment coefficient slope with center-of-gravity for each model

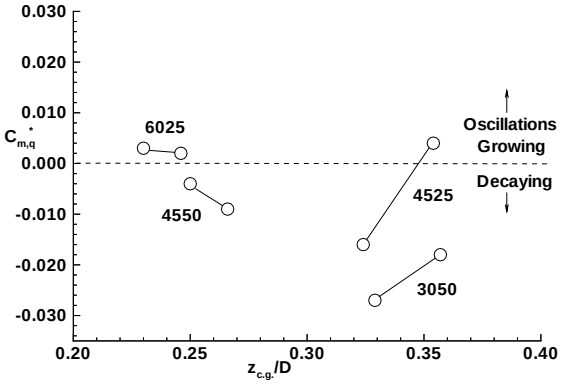

Fig. 13 Variation in damping parameter with center-of-gravity for each model